

High resolution X-ray study of supernova remnant J0453.6–6829 with unusually high forbidden-to-resonance ratio

Yosuke KOSHIBA,¹ Hiroyuki UCHIDA,¹ Takaaki TANAKA,² Yuki AMANO,¹
Hidetoshi SANO,³ and Takeshi Go TSURU¹

¹Department of Physics, Kyoto University, Kitashirakawa Oiwake-cho, Sakyo, Kyoto, Kyoto 606-8502, Japan

²Department of Physics, Konan University, 8-9-1 Okamoto, Higashinada, Kobe, Hyogo 658-8501, Japan

³National Astronomical Observatory of Japan, Mitaka, Tokyo 181-8588, Japan

*E-mail: koshiba.yosuke.b25@kyoto-u.jp

Received (reception date); Accepted (acceptation date)

Abstract

Recent high-resolution X-ray spectroscopy has revealed that several supernova remnants (SNRs) in the Large Magellanic Cloud (LMC) show unusually high forbidden-to-resonance (f/r) line ratios. While their origin is still uncertain and debated, most of these SNRs have asymmetric morphology and/or show evidence of interaction with dense material, which may hint at the true nature of the anomalous f/r ratios. Here we report on a detailed spectral analysis of an LMC SNR J0453.6–6829 with the Reflection Grating Spectrometer (RGS) on-board XMM-Newton. We find that the f/r ratio of O VII ($= 1.06^{+0.09}_{-0.10}$) is significantly higher than expected from the previously-reported thermal model. The spectrum is fairly explained by taking into account a charge exchange (CX) emission in addition to the thermal component. Analyzing archival ATCA & Parkes radio data, we also reveal that H I cloud is possibly interacting with J0453.6–6829. These results support the presence of CX in J0453.6–6829, as the origin of the obtained high f/r ratio. Although a contribution of the resonance scattering (RS) cannot be ruled out at this time, we conclude that CX seems more likely than RS considering the relatively symmetric morphology of this remnant.

Key words: atomic processes — ISM: supernova remnants — X-rays: individual (SNR J0453.6–6829) — X-rays: ISM

1 Introduction

Plasma diagnostics of astrophysical objects using line ratios of He-like ions (i.e., G and R ratios; Gabriel & Jordan 1969) will become a part of mainstream in the upcoming era of high-resolution X-ray spectroscopy. Recent grating observations revealed that several supernova remnants (SNRs) have anomalous line ratios of O VII, in which the forbidden line intensity relative to the resonance line (here-

after, f/r) is significantly higher than expected for an ordinary thermal plasma (e.g., Katsuda et al. 2011; Uchida et al. 2019). While their physical origin is still under debate, two interpretations have mainly been argued: charge exchange (CX) and resonance scattering (RS), both of which were predicted to occur in SNRs by previous calculations (e.g., Lallement 2004; Kaastra & Mewe 1995). The presence of the CX emission and/or RS effect would hinder accurate plasma diagnostics, and, more importantly, these

physical processes themselves work as useful probes to obtain key information such as collision and turbulent velocities. It is therefore required to know physical conditions and surrounding environments in which CX and/or RS can occur, that is, to reveal the origin of the anomalously high f/r ratios of OVII found in SNRs.

On the basis of observations with the Reflection Grating Spectrometer (RGS) onboard XMM-Newton, previous analyses of SNRs in the Large Magellanic Cloud (LMC) indicate that several of them tend to have relatively high f/r ratios of OVII; N23 (Broersen et al. 2011), N49 (Amano et al. 2020), and N132D (Suzuki et al. 2020). They are located in a dense ambient medium as suggested by radio-line (e.g., Banas et al. 1997; Sano et al. 2017) or infrared observations (e.g., Williams et al. 2006), which may hint at the cause of the anomalous spectral features. In this context, we found that no detailed spectroscopy has been performed so far for the middle-aged LMC SNR J0453.6–6829, although this remnant is in a dense environment similar to N23 and N132D according to Williams et al. (2006).

J0453.6–6829 is a relatively compact ($\sim 2'$ in diameter) remnant of a core-collapse explosion (Lopez et al. 2009; McEntaffer et al. 2012), containing a pulsar wind nebula (PWN) at the center of the shell (Gaensler et al. 2003). In addition to synchrotron radiation from the PWN, McEntaffer et al. (2012) indicated that the X-ray spectrum of J0453.6–6829 obtained with Chandra is well explained by a shock-heated interstellar medium (ISM). A similar conclusion was reached by Haberl et al. (2012), who performed multi-frequency observations of J0453.6–6829, including X-ray band with XMM-Newton. In their spectral fit, the forbidden line of OVII is seemingly higher than a normally expected thermal model. In this paper, we thus revisit the RGS data with particular attention to the He-like lines, in conjunction with an HI observation around the remnant, in order to investigate the relation between the f/r ratio and surrounding environment of J0453.6–6829. Errors are given at the 68% confidence level throughout the paper. We assume the distance to J0453.6–6829 to be 50 kpc (Pietrzyński et al. 2013).

2 Observation and data reduction

J0453.6–6829 was observed with XMM-Newton on 2001 March 29 (Obs. IDs 0062340101 and 0062340501). Since one of the data sets (Obs. ID 0062340501) was affected by large soft-proton flares, we present results only from Obs. ID 0062340101. The raw data were processed with the XMM Science Analysis Software (SAS) version 18.0.0 and the calibration data files released in 2020 June. In the

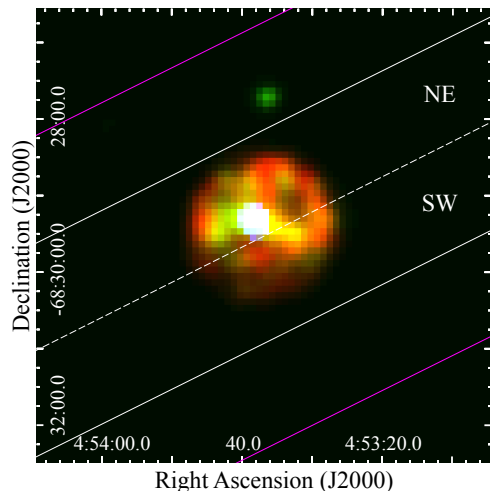


Fig. 1. True-color image of J0453.6–6829 obtained with EPIC (MOS and pn). Red, green, and blue correspond to the energy bands of 0.3–1.2 keV (soft), 1.2–2.0 keV (medium), and 2.0–8.0 keV (hard), respectively. The magenta lines indicate the cross dispersion width of the RGS ($5'$). The spectra and background are extracted from the region sandwiched by the white lines and the region above the source region sandwiched by the magenta and white lines, respectively. The dashed line shows how the source region is divided for a spatially-resolved analysis.

following spectral analysis, we combine RGS1 and RGS2 data with MOS spectra. After discarding periods of background flares, we obtained MOS and RGS data with effective exposure times of ~ 6 ks and ~ 20 ks, respectively. We do not analyze second order spectra because of their poor statistics.

3 Analysis and results

Figure 1 shows a background-subtracted true-color image of J0453.6–6829 taken by EPIC (MOS and pn). We extracted RGS spectra by limiting the cross-dispersion width so as to cover the whole of J0453.6–6829. MOS spectra were obtained from the entire region of the remnant. Off-source regions in the field of view (FOV) were used to extract background spectra for each instrument. We simultaneously fitted the unbinned RGS and MOS spectra using SPEX version 3.06.01 (Kaastra et al. 1996), applying a maximum likelihood method, W-stat (Wachter et al. 1979). Throughout this analysis, the hydrogen column density (N_H) of the Galactic absorption was fixed to $6 \times 10^{20} \text{ cm}^{-2}$ (Dickey & Lockman 1990) and that of the LMC was left free. We referred to Russell & Dopita (1992) for the elemental abundances of the LMC.

Figure 2 presents the MOS and RGS spectra of J0453.6–6829. McEntaffer et al. (2012) reported that the X-ray spectrum of J0453.6–6829 can be explained by a

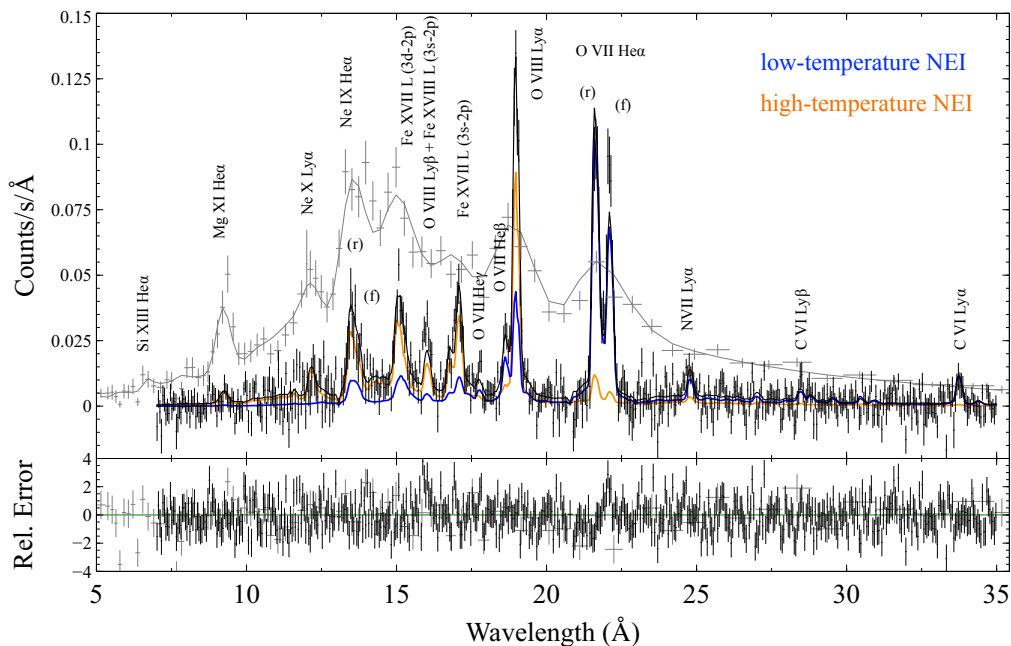


Fig. 2. RGS1+2 (black) and MOS1 (gray) spectra of J0453.6–6829. The colored solid curves indicate the contributions of the low-temperature (blue) and high-temperature NEI (orange) components. The bottom panel shows residuals from the best-fit model.

two-temperature non-equilibrium ionization (NEI) model (`neij`) with a power-law component for the PWN. We first applied this “2-NEI” model, in which photon index Γ and normalization of the power-law component were fixed to 2.0 and 3.5×10^{43} photons $\text{s}^{-1} \text{keV}^{-1}$ (McEntaffer et al. 2012), respectively. Free parameters for the thermal components include the electron temperature (kT_e), ionization timescale ($n_e t$, where n_e and t are the electron number density and the time after shock heating, respectively), and emission measure ($n_e n_H V$, where V is the emitting volume of the plasma). Abundances of C, N, O, Ne, Mg, Si, and Fe were set free and tied between the two components.

The best-fit model of the 2-NEI model is plotted in Figure 2, and its parameters are summarized in Table 1. We found that whereas the model can reproduce the MOS spectrum, significant residuals remain in the RGS spectrum especially at the O VII He α and O VIII Ly β lines. The result implies that some additional considerations are required to better explain the fine structures of the spectrum of J0453.6–6829. To clarify this point, we quantified the f/r intensity ratio of O VII by adding four Gaussians instead of multiplet line components of O VII He α , (i.e., resonance, forbidden and intercombination lines) implemented in the `neij` code: in this method, the other lines

and continua were not changed and were the same as those of the best-fit model. We compared the obtained value with that expected from the NEI model as indicated in Figure 3 (a). The resultant f/r ratio, $1.06^{+0.09}_{-0.10}$ requires $kT_e < 0.025$ keV. On the other hand, few O $^{6+}$ (He like) ions, which emit O VII, are present in such a low-temperature plasma (panel (b) of Figure 3), being inconsistent with our result. We thus conclude that any single or multiple NEI component(s) cannot reproduce the observed RGS spectrum. Another possible scenario to account for both f/r ratio and O VIII Ly β line is an over-ionized plasma. This scenario, however, would make a significant excess of radiative recombination continua, and thus contradicts the observed spectrum.

We next added a CX component to the 2-NEI model (hereafter, 2-NEI+CX model) to enhance the forbidden line intensity of O VII, as Uchida et al. (2019) did for a similar case of the Cygnus Loop. Free parameters of the CX model are normalization ($n_H n_{nh} V$, where n_{nh} is the density of the neutral materials) and shock velocity (zv). The ionization temperature was tied to kT_e of the low-temperature NEI component. The best-fit result and parameters are shown in Figure 4 and Table 1, respectively. As a result, we successfully fitted the RGS spectrum with the 2-NEI+CX model, except that the discrepancy be-

Table 1. Best-fit parameters of the J0453.6–6829 spectrum

| Component | Parameters (unit) | 2-NEI | 2-NEI+CX | 2-NEI–Gaus (RS) |
|--|---|------------------------|------------------------|------------------------|
| Absorption | $N_{\text{H(Galactic)}} (10^{20} \text{ cm}^{-2})$ | 6.0 (fixed) | 6.0 (fixed) | 6.0 (fixed) |
| | $N_{\text{H(LMC)}} (10^{20} \text{ cm}^{-2})$ | $8.7^{+2.8}_{-2.7}$ | $7.2^{+2.3}_{-2.4}$ | $6.9^{+5.2}_{-3.5}$ |
| Power law (PWN) | Normalization ($10^{44} \text{ photons s}^{-1} \text{ keV}^{-1}$) | 0.35 (fixed) | 0.35 (fixed) | 0.35 (fixed) |
| | Γ | 2.0 (fixed) | 2.0 (fixed) | 2.0 (fixed) |
| Low-temperature NEI | Emission Measure (10^{58} cm^{-3}) | 81^{+28}_{-20} | 60^{+13}_{-13} | 43^{+55}_{-25} |
| | kT_e (keV) | $0.15^{+0.01}_{-0.01}$ | $0.18^{+0.01}_{-0.02}$ | $0.15^{+0.05}_{-0.03}$ |
| | $n_e t$ ($10^{11} \text{ cm}^{-3} \text{ s}$) | > 10 | > 10 | > 10 |
| | C | $0.34^{+0.13}_{-0.10}$ | $0.40^{+0.15}_{-0.1}$ | $0.44^{+0.47}_{-0.17}$ |
| | N | $0.12^{+0.05}_{-0.04}$ | $0.15^{+0.07}_{-0.04}$ | $0.18^{+0.18}_{-0.06}$ |
| | O | $0.26^{+0.05}_{-0.04}$ | $0.23^{+0.05}_{-0.03}$ | $0.53^{+0.39}_{-0.10}$ |
| | Ne | $0.34^{+0.07}_{-0.05}$ | $0.33^{+0.08}_{-0.06}$ | $0.38^{+0.31}_{-0.07}$ |
| | Mg | $0.42^{+0.08}_{-0.07}$ | $0.41^{+0.13}_{-0.08}$ | $0.51^{+0.27}_{-0.09}$ |
| | Si | $0.22^{+0.09}_{-0.08}$ | $0.19^{+0.11}_{-0.07}$ | $0.32^{+0.20}_{-0.11}$ |
| | Fe | $0.25^{+0.04}_{-0.03}$ | $0.22^{+0.06}_{-0.03}$ | $0.25^{+0.06}_{-0.04}$ |
| High-temperature NEI | Emission Measure (10^{58} cm^{-3}) | 12^{+5}_{-4} | $7.9^{+7.9}_{-3.5}$ | 17^{+10}_{-16} |
| | kT_e (keV) | $0.42^{+0.05}_{-0.03}$ | $0.48^{+0.09}_{-0.08}$ | $0.35^{+0.33}_{-0.08}$ |
| | $n_e t$ ($10^{11} \text{ cm}^{-3} \text{ s}$) | $1.6^{+0.5}_{-0.3}$ | $1.4^{+0.5}_{-0.3}$ | > 2.2 |
| CX | Emission Measure (10^{58} cm^{-3}) | ... | 18^{+100}_{-9} | ... |
| | v_{col} (km s^{-1}) | ... | < 286 | ... |
| Negative Gaussian*: NeIX He α (r) | Normalization ($10^{44} \text{ photons s}^{-1}$) | ... | ... | $< 8.8 \times 10^{-2}$ |
| | FeXVII L(3d-2p) | ... | ... | 0.14 ± 0.09 |
| | FeXVII L(3s-2p) | ... | ... | < 0.31 |
| | O VIII Ly α | ... | ... | $2.3^{+1.2}_{-0.6}$ |
| | O VII He α (r) | ... | ... | $1.9^{+0.6}_{-0.4}$ |
| W-statistic/d.o.f. | | 4124/3627 | 4107/3625 | 4085/3622 |

* The line centroid wavelengths of the Gaussians at NeIX He α (r), FeXVII L(3d-2p), FeXVII L(3s-2p), O VIII Ly, and O VII He α (r) are fixed to 13.4 Å, 15.0 Å, 17.0 Å, 18.9 Å, and 21.6 Å, respectively.

tween the data and model is still seen at the O VIII Ly β line.

A similar excess of the O VIII Ly β line has been reported by Amano et al. (2020), who analyzed the RGS spectrum of N49 and concluded that the line ratios including f/r of O VII can be reasonably explained by taking into account the effect of RS. We thus applied negative Gaussians in addition to the 2-NEI model (hereafter, 2-NEI–Gaus model), in which we assumed that the SNR shell is a slab and all scattered photons will escape from the line of sight (Kaastra & Mewe 1995). The Gaussians were fixed at the centroid wavelengths of the lines whose oscillator strengths are relatively large: resonance lines of NeIX and O VII, FeXVII L(3d-2p), FeXVII L(3s-2p), and O VIII Ly α . Normalizations (photons s^{-1}) of these five Gaussians were set free and the other parameters are the same as the 2-NEI model. As shown in Figure 4, the 2-NEI–Gaus model globally reduces the residuals. The best-fit parameters (Table 1) are consistent with those expected for a typical middle-aged SNR. We therefore claim that a presence of RS cannot be ruled out in terms of the spectral fitting.

4 Discussion

As indicated in the previous section, the high-resolution X-ray spectrum of J0453.6–6829 suggests the presence of CX or RS in the remnant. Similar cases have often been discussed in the literature (e.g., Uchida et al. 2019; Amano et al. 2020; Suzuki et al. 2020). Although it is in general difficult to distinguish between these two possibilities with the available spectroscopies, the SNR morphology and surrounding environment may provide a clue to the true origin of the high f/r ratio. In Table 2, we summarize LMC/SMC SNRs for which the f/r (or G) ratios were measured so far using the RGS to compare our results with those from other SNRs in the discussion below.

4.1 X-ray Morphology of J0453.6–6829

For quantitative evaluation of the effect of RS, we calculated a transmission factor τ by applying the same method as Amano et al. (2020). We compared theoretical values of τ for several optical depths according to Kaastra & Mewe (1995) with those estimated from the best-fit normalizations of the negative Gaussians. Figure 5 shows the result. Although the model fails to explain the observed resonance

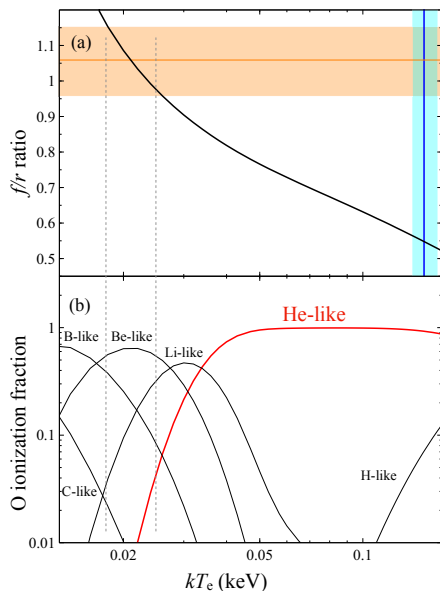


Fig. 3. (a) f/r ratio of O VII He α as a function of electron temperature kT_e in the case of the best-fit value of $n_e t$ of the low-temperature NEI component. The horizontal orange and vertical blue hatched areas indicate the observed line ratio and kT_e of the low-temperature NEI component, respectively. The curve represents theoretically expected values calculated from the `neij` model in SPEX. (b) Oxygen ionization fraction as a function of kT_e .

line of Ne IX, the estimated τ for J0453.6–6829 are roughly consistent with those at $N_H = 1.0\text{--}5.0 \times 10^{19} \text{ cm}^{-2}$, which corresponds to a plasma depth of 3–18 pc under an assumption of the plasma density $n_H = 1.1 \text{ cm}^{-3}$ (Williams et al. 2006). Since the diameter of J0453.6–6829 is estimated to be ~ 36 pc from the apparent angular size of the shell ($\sim 2.5'$), the line-of-sight plasma depth that contributes to RS should be 10–50% of the diameter. If this is really the case, the shell-type SNR would be required to have a highly asymmetric morphology; for instance, a bright shell is prominent only on one side of the remnant (see Figure 6).

If J0453.6–6829 has an ideal spherical symmetric structure, the RS effect will be cancelled out and an enhancement of f/r will not occur. Note that the RGS spectrum of J0453.6–6829 was obtained from the entire region. We can thus postulate that asymmetry of an SNR is a key parameter to evaluate the effect of RS. From a soft-band imaging analysis by Lopez et al. (2011), we found that J0453.6–6829 has a less asymmetric morphology among the six SNRs listed in Table 2. Other core-collapse remnants are more “elliptical” (N23) or “non-uniform” (N132D), which are parametrized as P_2/P_0 and P_3/P_0 in their calculation. Although N49 was not analyzed by Lopez et al. (2011), it would also be categorized as a highly elliptical remnant due to its morphology similar to

that of N23. It is reasonable that N23, N49, and N132D show relatively high f/r ratios due to RS, as claimed by previous studies (Broersen et al. 2011; Amano et al. 2020; Suzuki et al. 2020). On the other hand, in the case of J0453.6–6829, the effect of RS might be unlikely or insufficient to satisfactorily explain the observed high f/r ratio.

4.2 Surrounding Environment of J0453.6–6829

CX is another possibility that causes the enhancement of f/r . An interaction with a dense ambient medium is expected in this case, as in previous studies of Galactic SNRs with the RGS: Puppis A (Katsuda et al. 2012) and the Cygnus Loop (Uchida et al. 2019). While McEntaffer et al. (2012) implied a presence of dense gas in the vicinity of J0453.6–6829 because of a spatial correlation between the X-ray and infrared morphologies, the surrounding environment of this remnant has still been unclear (Williams et al. 2006; Lakićević et al. 2015). As shown in Figure 7, we compared the ATCA & Parkes (Kim et al. 2003) HI velocity channel map around J0453.6–6829 with the X-ray morphology and found HI clouds located along with the southwestern half of J0453.6–6829. Figure 8 shows the integrated intensity maps of HI. We also found the southwestern part of the remnant is increasingly covered with an HI cloud. The position-velocity diagram suggests that the SNR shell is expanding into the dense gas (panel (b) of Figure 8).

If the SNR shell interacts with the HI cloud in the southwestern region, relatively strong forbidden line emission would be detected there. We thus divided the data into two in the cross-dispersion direction (namely, northeast; NE and southwest; SW) as indicated in Figure 1. As displayed in Figure 9, the forbidden line intensity of O VII in SW is stronger than that in NE. Applying the same method as the entire region, we obtained f/r ratios of $0.97^{+0.18}_{-0.14}$ and $1.41^{+0.40}_{-0.29}$ for NE and SW, respectively. Although statistically they are equal within the errors, the trend is consistent with the above expectation and thus strongly supports the presence of CX. The best-fit models of 2-NEI+CX for these regions are displayed in Figure 10. The model parameters are given in Table 3. While the CX component is required both in NE and SW, its contribution is relatively dominant in SW. We thus confirmed that the anomalous f/r ratios is due to the CX emission, mainly caused by an interaction with the southwestern HI cloud.

According to the discussion above, we presume that the emitting region of CX is the southwestern edge of J0453.6–6829, which is in contact with the HI cloud.

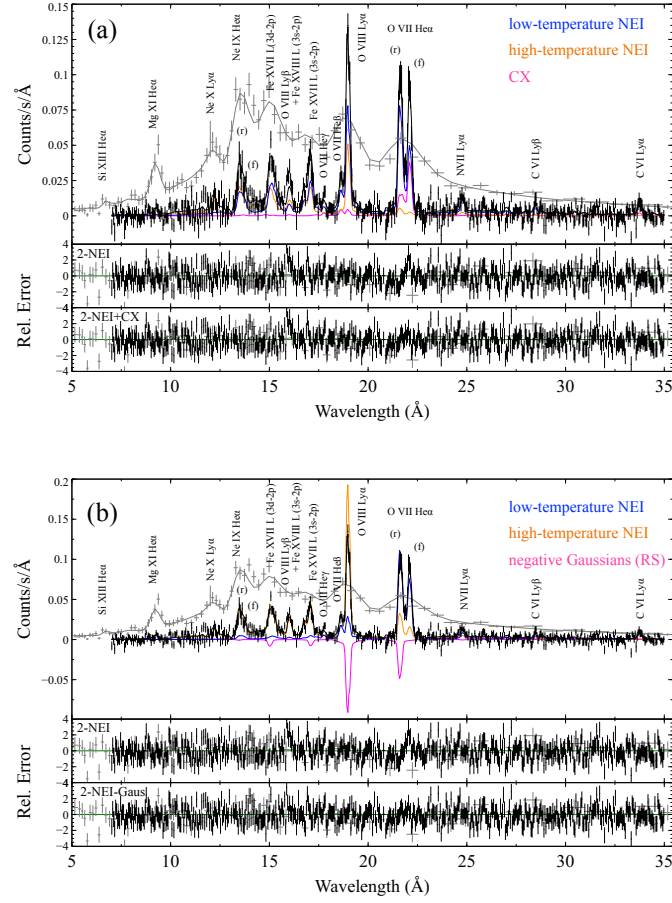


Fig. 4. (a) Same as Figure 2 but with the 2-NEI+CX model. The magenta curve represents the CX component. The middle and lower panels show residuals from the 2-NEI and 2-NEI+CX models, respectively. (b) Same as Figure 2 but with the 2-NEI-Gaus model. The magenta curve indicates scattered line intensities. The middle and lower panels show residuals from the 2NEI and 2-NEI-Gaus models, respectively.

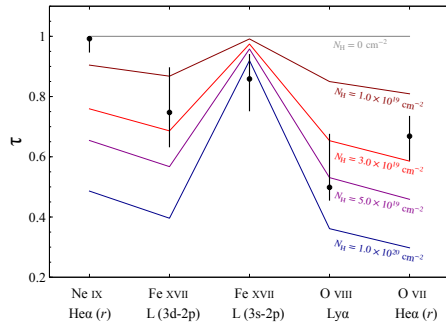


Fig. 5. Transmission factors τ for each line. The black points are those estimated from the observed line intensities and normalizations of the negative Gaussians. The colored curves represent expected values of τ as a function of N_H .

To quantitatively examine the possibility of CX, we estimate the emitting volume V_{CX} using the volume emis-

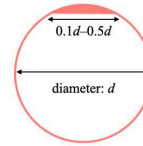


Fig. 6. Example schematic view of an X-ray emitting plasma that accounts for the result of the calculation of RS.

sion measure of the CX component $EM_{CX} = n_H n_{nh} V_{CX}$, where n_{nh} is the neutral material density of the surrounding gas. Given that the H I gas has a typical density of $n_{nh} = 10 \text{ cm}^{-3}$, we obtain the emitting volume V_{CX} to be $2 \times 10^{58} \text{ cm}^3$. Since the total volume of J0453.6–6829 is estimated to be $V_{SNR} \sim 10^{60} \text{ cm}^3$ assuming a diameter of $\sim 36 \text{ pc}$, we conclude that the CX occurs in $\sim 0.4\%$ of the SNR radius. The result fits well with the calculation by Lallement (2004) and thus supports the possibility that the observed anomalous f/r ratio is due to CX. Note that the

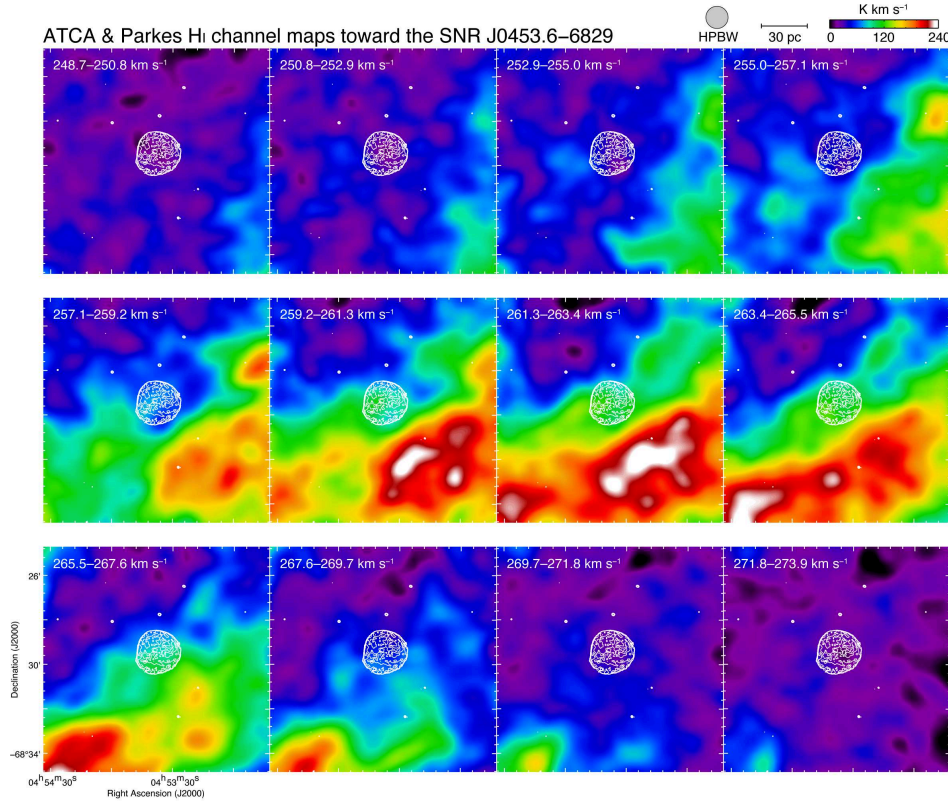


Fig. 7. ATCA & Parkes H I channel maps overlaid with the Chandra X-ray intensity of J0453.6–6829 (white contours). Each panel shows the H I intensity map integrated over the 2.1 km s^{-1} width evenly spaced in the $248.7\text{--}273.9 \text{ km s}^{-1}$ range.

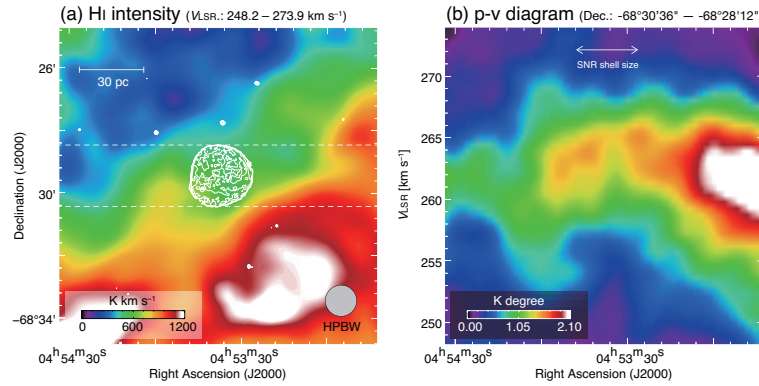


Fig. 8. (a) Integrated intensity map of the ATCA & Parkes H I in V_{LSR} of $248.2\text{--}273.9 \text{ km s}^{-1}$. (b) Position-velocity diagram of H I image. The integration range in Dec. is from $-68^\circ 30' 36''$ to $-68^\circ 28' 12''$ (J2000.0). The white arrow indicates the position of J0453.6–6829.

significant residuals seen at $\sim 16 \text{ \AA}$ (section 3) is still an open question; such discrepancies around the O VIII Ly β line are often pointed out by many RGS observations (e.g., Amano et al. 2020), and might be due to uncertainties in the atomic data (see also, de Plaa et al. 2012).

5 Conclusions

We performed a high-resolution spectroscopy of J0453.6–6829 with the RGS onboard XMM-Newton and found that the intensity of the forbidden line of O VII is significantly stronger than expected from a simple thermal (2-NEI) model. To account for the obtained high f/r ratio ($1.06^{+0.09}_{-0.10}$), we examined two possibilities: CX and RS, which have been proposed for explaining similar spectral features found in SNRs. Both models are

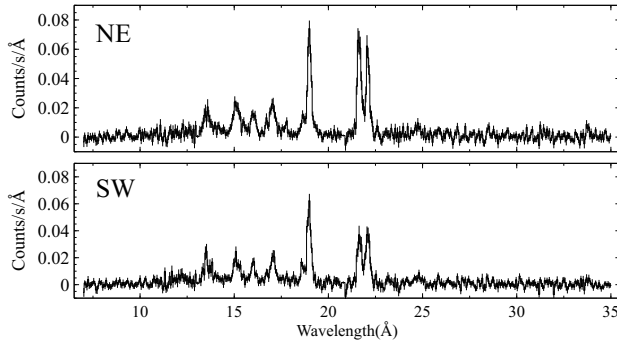


Fig. 9. RGS1+2 spectra of the NE (top) and SW (bottom) regions of J0453.6–6829.

statistically acceptable, although small residuals remain at ~ 16 Å (around the O VIII Ly β line) between the data and the 2-NEI+CX model. Such discrepancies are often pointed out by many RGS observations (e.g., de Plaa et al. 2012; Amano et al. 2020) and are likely due to uncertainties in the atomic data. From the best-fit result with the RS model, we estimated a transmission factor τ ; the result requires a significantly asymmetric shape along the line of sight. This may be inconsistent with the apparent morphology of J0453.6–6829, since a previous systematic X-ray study indicates that this remnant is one of the “least asymmetric” core-collapse SNRs (Lopez et al. 2011). On the other hand, our estimate of the emitting volume for the CX component ($\sim 0.4\%$ of the SNR radius) agrees well with a theoretical expectation (Lallement 2004). We also found evidence of an interaction between J0453.6–6829 and the dense ambient gas in the ATCA & Parkes H I map, which supports the picture that the observed f/r ratio is due to the CX emission at SNR shock fronts. In conclusion, the presence of CX in J0453.6–6829 is favored in our study, while a slight or significant contribution of the RS effect also cannot be ruled out. Future spatially resolved spectroscopies with high angular resolution missions like Athena will clarify this point.

Acknowledgments

We thank Brian J. Williams for a helpful discussion about the previous multiwavelength studies of the SNR J0453.6–6829. The ATCA and the Parkes radio telescope are all part of the Australia Telescope National Facility, which is funded by the Australian Government for operation as a National Facility managed by CSIRO. We acknowledge the Gomeroi and Wiradjuri people as the traditional owners of the Observatory sites. This work is supported by JSPS/MEXT KAKENHI Scientific Research Grant Numbers JP19K03915 (H.U.), JP19H01936 (T.T.), JP19K14758 (H.S.), JP20KK0309 (H.S.), and JP21H04493 (T.G.T. and T.T.).

References

- Amano, Y., Uchida, H., Tanaka, T., et al. 2020, *ApJ*, 897, 12.
 Banas, K. R., Hughes, J. P., Bronfman, L., et al. 1997, *ApJ*, 480, 607.
 Bhardwaj, A., Elsner, R. F., Randall Gladstone, G., et al. 2007, *Planet. Space Sci.*, 55, 1135.
 Blair, W. P., Morse, J. A., Raymond, J. C., et al. 2000, *ApJ*, 537, 667.
 Broersen, S., Vink, J., Kaastra, J., et al. 2011, *A&A*, 535, A11.
 Chevalier, R. A. 2005, *ApJ*, 619, 839.
 Chu, Y.-H. & Kennicutt, R. C. 1988, *AJ*, 96, 1874.
 Cravens, T. E. 2002, *Science*, 296, 1042.
 de Plaa, J., Zhuravleva, I., Werner, N., et al. 2012, *A&A*, 539, A34.
 Dickey, J. M. & Lockman, F. J. 1990, *ARA&A*, 28, 215.
 Gabriel, A. H. & Jordan, C. 1969, *MNRAS*, 145, 241.
 Gaensler, B. M., Hendrick, S. P., Reynolds, S. P., et al. 2003, *ApJL*, 594, L111.
 Ghavamian, P., Rakowski, C. E., Hughes, J. P., et al. 2003, *ApJ*, 590, 833.
 Haberl, F., Filipović, M. D., Bozzetto, L. M., et al. 2012, *A&A*, 543, A154.
 Hester, J. J. & Cox, D. P. 1986, *ApJ*, 300, 675.
 Hitomi Collaboration, Aharonian, F., Akamatsu, H., et al. 2018, *PASJ*, 70, 10.
 Hughes, J. P., Hayashi, I., & Koyama, K. 1998, *ApJ*, 505, 732.
 Hughes, J. P., Rakowski, C. E., & Decourchelle, A. 2000, *ApJL*, 543, L61.
 Hughes, J. P., Rafelski, M., Warren, J. S., et al. 2006, *ApJL*, 645, L117.
 Kaastra, J. S. & Mewe, R. 1995, *A&A*, 302, L13.
 Kaastra, J. S., Mewe, R., & Nieuwenhuijzen, H. 1996, *UV and X-ray Spectroscopy of Astrophysical and Laboratory Plasmas*, 411.
 Katsuda, S., Tsunemi, H., Mori, K., et al. 2011, *ApJ*, 730, 24.
 Katsuda, S., Tsunemi, H., Mori, K., et al. 2012, *ApJ*, 756, 49.
 Kim, S., Staveley-Smith, L., Dopita, M. A., et al. 2003, *ApJS*, 148, 473.
 Lakićević, M., van Loon, J. T., Meixner, M., et al. 2015, *ApJ*, 799, 50.
 Lallement, R. 2004, *A&A*, 422, 391.
 Law, C. J., Milisavljevic, D., Patnaude, D. J., et al. 2020, *ApJ*, 894, 73.
 Levenson, N. A., Graham, J. R., Keller, L. D., et al. 1998, *ApJS*, 118, 541.
 Long, K. S., Bamba, A., Aharonian, F., et al. 2014, *arXiv:1412.1166*.
 Lopez, L. A., Ramirez-Ruiz, E., Badenes, C., et al. 2009, *ApJL*, 706, L106.
 Lopez, L. A., Ramirez-Ruiz, E., Huppenkothen, D., et al. 2011, *ApJ*, 732, 114.
 McEntaffer, R. L., Brantseg, T., & Presley, M. 2012, *ApJ*, 756, 17.
 Miyata, E., Masai, K., & Hughes, J. P. 2008, *PASJ*, 60, 521.
 Park, S., Burrows, D. N., Garmire, G. P., et al. 2003, *ApJ*, 586, 210.
 Petre, R., Kriss, G. A., Winkler, P. F., et al. 1982, *ApJ*, 258, 22.

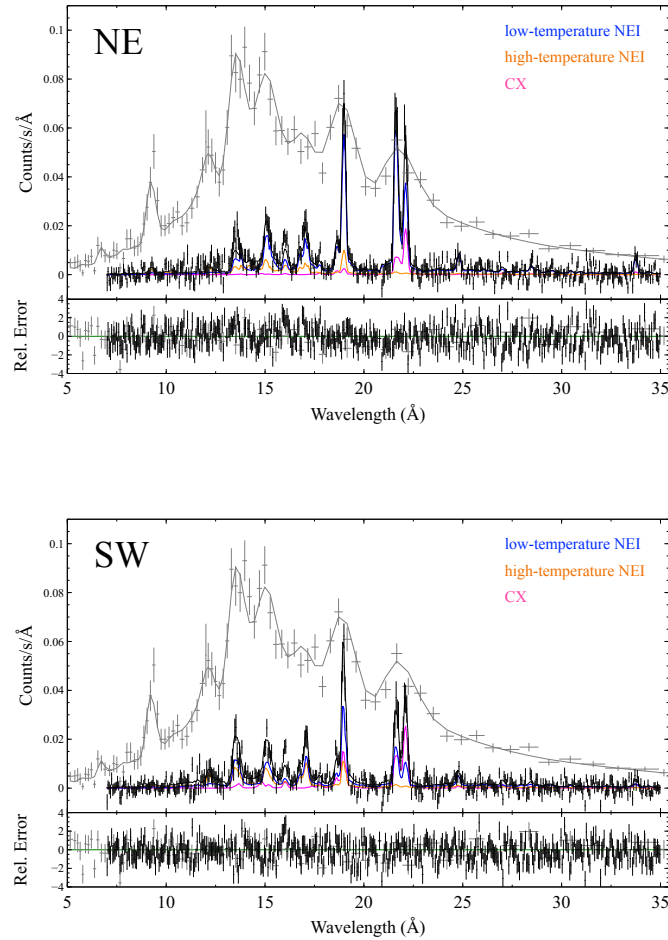


Fig. 10. (a) Same as the panel (a) of Figure 2 but for the NE (top) and SW (bottom) regions.

- Pietrzyński, G., Graczyk, D., Gieren, W., et al. 2013, *Nature*, 495, 76.
- Rasmussen, A. P., Behar, E., Kahn, S. M., et al. 2001, *A&A*, 365, L231.
- Russell, S. C. & Dopita, M. A. 1992, *ApJ*, 384, 508.
- Sano, H., Fukui, Y., Yoshiike, S., et al. 2015, *Revolution in Astronomy with ALMA: The Third Year*, 499, 257
- Sano, H., Fujii, K., Yamane, Y., et al. 2017, *6th International Symposium on High Energy Gamma-Ray Astronomy*, 1792, 040038.
- Sano, H., Plucinsky, P. P., Bamba, A., et al. 2020, *ApJ*, 902, 53.
- Schenck, A., Park, S., & Post, S. 2016, *AJ*, 151, 161.
- Someya, K., Bamba, A., & Ishida, M. 2010, *PASJ*, 62, 1301.
- Suzuki, H., Yamaguchi, H., Ishida, M., et al. 2020, *ApJ*, 900, 39.
- Tuohy, I. R. & Dopita, M. A. 1983, *ApJL*, 268, L11.
- Uchida, H., Koyama, K., & Yamaguchi, H. 2015, *ApJ*, 808, 77.
- Uchida, H., Katsuda, S., Tsunemi, H., et al. 2019, *ApJ*, 871, 234.
- van der Heyden, K. J., Bleeker, J. A. M., Kaastra, J. S., et al. 2003, *A&A*, 406, 141.
- Vogt, F. & Dopita, M. A. 2011, *Ap&SS*, 331, 521.
- Wachter, K., Leach, R., & Kellogg, E. 1979, *ApJ*, 230, 274.
- Williams, B. J., Borkowski, K. J., Reynolds, S. P., et al. 2006, *ApJL*, 652, L33.
- Winkler, P. F., Tuttle, J. H., Kirshner, R. P., et al. 1988, *IAU Colloq. 101: Supernova Remnants and the Interstellar Medium*, 65
- Xu, H., Kahn, S. M., Peterson, J. R., et al. 2002, *ApJ*, 579, 600.
- Yamane, Y., Sano, H., van Loon, J. T., et al. 2018, *ApJ*, 863, 55.

Table 2. f/r ratios or G -ratios for O VII He α

| Name | Type of SNe | Ref. Type* | Age (yr) | Ref. Age* | f/r or G ratios | Ref. Ratios* | Surrounding environments | Ref. Surrounding environments* |
|-----------------|-----------------------------|---------------|-------------|--------------|---------------------------------------|-----------------|-----------------------------|-----------------------------------|
| 1E 0102–7219 | Ib/c or III _L /b | 1, 2 | 1000 | 3 | $0.55^{\ddagger} \pm 0.03$ | 4 | no data | |
| N132D | Ib | 1 | 2500 | 5 | $0.68^{\ddagger} \pm 0.02$ | 6 | CO and H I clouds | 7, 8, 9 |
| DEM L71 | Ia | 10 | 4400 | 11 | 0.65^{\ddagger} | 12 | no data | |
| N23 (0506–68.0) | II | 13 | 4600 | 13 | $0.99^{\ddagger} \pm 0.06$ | 14 | star-forming region | 15 |
| N49 | II | 16 | 6600 | 17 | $1.23^{\ddagger} \pm 0.12$ | 18 | CO and H I clouds | 7, 8, 19 |
| J0453.6–6829 | II | 20 | 13000 | 21 | $1.06^{\ddagger} \pm 0.09$ -0.10 | 22 | H I clouds | 22 |

* References. (1) Blair et al. (2000); (2) Chevalier (2005); (3) Hughes et al. (2000); (4) Rasmussen et al. (2001); (5) Vogt & Dopita (2011); (6) Suzuki et al. (2020); (7) Banas et al. (1997); (8) Sano et al. (2017); (9) Sano et al. (2020); (10) Hughes et al. (1998); (11) Ghavamian et al. (2003); (12) van der Heyden et al. (2003); (13) Hughes et al. (2006); (14) Broersen et al. (2011); (15) Chu & Kennicutt (1988); (16) Uchida et al. (2015); (17) Park et al. (2003); (18) Amano et al. (2020); (19) Yamane et al. (2018); (20) Lopez et al. (2009); (21) Gaensler et al. (2003); (22) This work.

‡ f/r ratio ‡ G ratio ($f+i$)/ r

Table 3. Best-fit parameters of the NE and SW spectra

| Component | Parameters (unit) | 2-NEI+CX | |
|----------------------|---|------------------------|------------------------|
| | | NE | SW |
| Absorption | $N_{\text{H(Galactic)}} (10^{20} \text{ cm}^{-2})$ | 6.0 (fixed) | |
| | $N_{\text{H(LMC)}} (10^{20} \text{ cm}^{-2})$ | $7.0^{+2.3}_{-3.4}$ | $6.3^{+3.3}_{-2.5}$ |
| Power law (PWN) | Normalization ($10^{44} \text{ photons s}^{-1} \text{ keV}^{-1}$) | 0.35 (fixed) | |
| | Γ | 2.0 (fixed) | |
| Low-temperature NEI | Emission Measure (10^{58} cm^{-3}) | 100^{+25}_{-48} | 33^{+14}_{-17} |
| | kT_e (keV) | $0.20^{+0.04}_{-0.01}$ | 0.21 ± 0.01 |
| | $n_{\text{et}} (10^{11} \text{ cm}^{-3} \text{ s})$ | > 2 | > 0.6 |
| | C | 0.6 ± 0.2 | 0.2 ± 0.1 |
| | N | 0.3 ± 0.1 | $0.17^{+0.06}_{-0.07}$ |
| | O | $0.27^{+0.06}_{-0.07}$ | $0.17^{+0.04}_{-0.05}$ |
| | Ne | 0.4 ± 0.1 | $0.29^{+0.06}_{-0.08}$ |
| | Mg | 0.5 ± 0.1 | $0.39^{+0.08}_{-0.09}$ |
| | Si | 0.3 ± 0.1 | $0.2^{+0.2}_{-0.1}$ |
| | Fe | $0.24^{+0.06}_{-0.05}$ | 0.16 ± 0.04 |
| High-temperature NEI | Emission Measure (10^{58} cm^{-3}) | 8^{+6}_{-2} | 8^{+21}_{-3} |
| | kT_e (keV) | $0.59^{+0.09}_{-0.10}$ | $0.37^{+0.07}_{-0.09}$ |
| | $n_{\text{et}} (10^{11} \text{ cm}^{-3} \text{ s})$ | $1.7^{+3.6}_{-0.6}$ | > 3 |
| CX | Emission Measure (10^{58} cm^{-3}) | 16^{+75}_{-14} | 20^{+27}_{-9} |
| | $v_{\text{col}} (\text{km s}^{-1})$ | < 250 | 350^{+180}_{-130} |
| W-statistic/d.o.f. | | 4108/3625 | 4107/3625 |